Search for inelastic WIMP nucleus scattering on ^{129}Xe in data from the XMASS-I experiment

H. Uchida[8,*], K. Abe[1,3], K. Hieda[1], K. Hiraide[1,3], S. Hirano[1], K. Ichimura[1], Y. Kishimoto[1,3], K. Kobayashi[1,3], S. Moriyama[1,3], K. Nakagawa[1], M. Nakahata[1,3], H. Ogawa[1,3], N. Oka[1], H. Sekiya[1,3], A. Shinozaki[1], Y. Suzuki[1,3], A. Takeda[1,3], O. Takachio[1], D. Umemoto[1], M. Yamashita[1,3], B. S. Yang[1], S. Tasaka[2], J. Liu[3], K. Martens[3], K. Hosokawa[5], K. Miuchi[5], A. Murata[5], Y. Onishi[5], Y. Otsuka[5], Y. Takeuchi[5,3], Y. H. Kim[6], K. B. Lee[6], M. K. Lee[6], J. S. Lee[6], Y. Fukuda[7], Y. Itow[8,4], K. Masuda[8], Y. Nishitani[8], H. Takiya[8], N. Y. Kim[9], Y. D. Kim[9], F. Kusaba[10], K. Nishijima[10], K. Fujii[11], I. Murayama[11], and S. Nakamura[11]

[1]*Kamioka Observatory, Institute for Cosmic Ray Research, the University of Tokyo, Higashi-Mozumi, Kamioka, Hida, Gifu 506-1205, Japan*
[2]*Information and Multimedia Center, Gifu University, Gifu 501-1193, Japan*
[3]*Kavli Institute for the Physics and Mathematics of the Universe (WPI), the University of Tokyo, Kashiwa, Chiba 277-8582, Japan*
[4]*Kobayashi-Maskawa Institute for the Origin of Particles and the Universe, Nagoya University, Furo-cho, Chikusa-ku, Nagoya, Aichi 464-8602, Japan*
[5]*Department of Physics, Kobe University, Kobe, Hyogo 657-8501, Japan*
[6]*Korea Research Institute of Standards and Science, Daejeon 305-340, South Korea*
[7]*Department of Physics, Miyagi University of Education, Sendai, Miyagi 980-0845, Japan*
[8]*Solar-Terrestrial Environment Laboratory, Nagoya University, Nagoya, Aichi 464-8601, Japan*
[9]*Department of Physics, Sejong University, Seoul 143-747, South Korea*
[10]*Department of Physics, Tokai University, Hiratsuka, Kanagawa 259-1292, Japan*
[11]*Department of Physics, Faculty of Engineering, Yokohama National University, Yokohama, Kanagawa 240-8501, Japan*
*E-mail: xmass.publications@km.icrr.u-tokyo.ac.jp

....
A search for inelastic scattering of weakly interacting massive particles (WIMPs) on the isotope ^{129}Xe was done in data taken with the single-phase liquid-xenon detector XMASS at the Kamioka Observatory. Using a restricted volume containing 41 kg of liquid xenon at the very center of our detector, we observed no significant excess of events in 165.9 live days of data. Our background reduction allowed us to derive our limits without explicitly subtracting the remaining events that are compatible with background expectations. As an example, we derive for a 50 GeV WIMP an upper limit of 3.2 pb at the 90% confidence level for its inelastic cross section on ^{129}Xe nuclei.
....
Subject Index   C43, E64, F41

1. Introduction

There is ample observational evidence for the existence of dark matter in the Universe. All evidence is gravitational though: we derive its presence by observing the distribution and motion of normal matter in galaxies and clusters. No evidence exists for any interaction, other than gravitational, that dark matter might have with normal matter. Theory, however, provides strong motivation to postulate

weakly interacting massive particle (WIMP) dark matter. If WIMPs do indeed make up the bulk of the dark matter in the Universe and its weak coupling to normal matter is strong enough, elastic scattering of nuclei should provide the experimental signature for such an interaction. Unfortunately, the resulting recoil energy is very low ($\sim$10 keV), and the spectrum of the recoiling nuclei falls off exponentially, making it difficult to distinguish from backgrounds near the detector threshold.

All around the world, significant experimental effort is being expended to probe for such nuclear recoils through elastic scattering [1–9]. Inelastic scattering that excites low-lying nuclear states in suitable target nuclei provides another avenue to probe for WIMP dark matter. Its advantage is that nuclear excited states and their de-excitation mechanisms are typically well measured, and thus the expected energy deposit in the detector is known, resulting in the readily identifiable signature of a line in the energy spectrum.

Experimental searches have been done with ^{127}I, which has a suitable nuclear excitation level at 57.6 keV [10,11]. Among the xenon isotopes found in naturally occurring xenon, ^{129}Xe has the lowest-lying excited nuclear state at 39.58 keV and with 26.4% has almost the highest natural abundance; the runner-up would be ^{131}Xe with 21.2% abundance and an 80.19 keV excitation. Thus the ^{129}Xe excitation threshold is lower than that for ^{127}I, yet significantly above both the XMASS data acquisition and analysis thresholds. The de-excitation of this M1 state in ^{129}Xe proceeds through gamma-ray emission or an internal conversion electron with subsequent X-ray emission. With its high nuclear charge, Xe itself is a good absorber for such gamma-rays, providing liquid-xenon (LXe) detectors with an intrinsically high detection efficiency for the prospective signal.

So far, the DAMA group has searched for this signal in a 2500 kg day exposure of 6.5 kg of LXe. They used 99.5% enriched ^{129}Xe and constrained the inelastic cross section for 50 GeV WIMPs to be less than 3 pb at the 90% confidence level (C.L.) [12,13].

In this paper, the results from our own search for this signal in XMASS data are reported. Though the LXe in XMASS contains ^{129}Xe only at the level of its natural abundance, our detector's significantly lower background in its fiducial volume, which is a spherical volume around the center of the detector, and excellent light yield result in a high sensitivity for this inelastic scattering signal.

2. The XMASS detector

The XMASS experiment is located underground in the Kamioka Observatory at a depth of 2700 m.w.e., aiming to detect dark matter [14]. XMASS is a single-phase liquid-xenon scintillation detector containing 1050 kg of Xe in its oxygen free high conductivity copper vessel. Xenon scintillation light is detected by 642 inward-pointing Hamamatsu R10789 series photomultiplier tubes (PMTs) arranged on an 80 cm diameter pentakis-dodecahedron support structure within the LXe containment vessel to give a total photocathode coverage of 62.4% of the detector's inner surface. This surface encloses an active target region containing 835 kg of liquid xenon.

To shield the scintillator volume from external gamma-rays and neutrons, and to veto muon-induced backgrounds, this active target of our detector is located at the center of a ϕ 10 m $\times$ 11 m cylindrical tank filled with pure water. This water volume is viewed by 72 Hamamatsu R3600 20-inch PMTs to provide an active muon veto as well as being a passive shield against external backgrounds. This is the first time that a water Cherenkov shield has been used in a direct dark matter search.

Radioactive calibration sources can be inserted through a portal above the center of the detector and positioned along the central vertical axis of the inner detector to calibrate energy as well as position reconstruction. Measuring with a ^{57}Co source from the center of the detector volume, the

photoelectron yield[1] is determined to be 13.9 photoelectrons (p.e.)/keV. A more detailed description of the XMASS detector is presented in Ref. [15].

PMT signals are passed though preamplifiers with a gain of 11 before being processed by analog timing modules (ATMs) [16]. These modules combine the functions of typical ADC and TDC modules, recording both the integrated charge and the arrival time of each PMT signal. For each PMT channel, the discriminator threshold is set to $-5\,$mV, which corresponds to 0.2 p.e. When a PMT signal exceeds this threshold, a "hit" is registered on the channel. A global trigger is generated if the number of hit PMTs within a 200 ns window is more than nine.

A complete XMASS detector Monte Carlo (MC) simulation package based on Geant4 [17,18] including a simulation of the readout electronics has been developed [15] and is used in our analysis. The simulation has been tuned using calibration data, and the optical properties of the liquid xenon have also been extracted from the calibration data. The energy dependence of the light yield as well as the energy resolution were also tuned on calibration data, as were the decay constant of gamma-induced scintillation light and the transit timing spread (TTS) of the PMTs. We choose these constants so that we can reproduce the observed distribution of PMT hit timings in our simulation. The effective decay constant τ_γ thus determined is 27.3 ns for a 39.58 keV gamma-ray and the TTS is 2.33 ns (rms). The manufacturer-evaluated TTS for our PMTs is 2.4 ns. For τ_γ, Ref. [19] reports 34 ns but, as our simulation reproduces the observed timing distribution for various gamma sources at both lower and higher energies, we do not consider this the only known outside measurement in our evaluation of systematic uncertainty.

3. Expected signal and detector simulation

A WIMP on ^{129}Xe inelastic scattering produces a 39.58 keV γ-ray from nuclear de-excitation plus a few keV energy deposition from the recoil of the ^{129}Xe nucleus. Energy spectra for the nuclear recoil part are obtained by simulation, just as in Refs. [12,13]. The differential rate for inelastic scattering of WIMPs on nucleons here, as in these references, is calculated according to:

$$\frac{dR}{dE_{\text{det}}} = \frac{dE_{\text{nr}}}{d(\mathcal{L}_{\text{eff}}E_{\text{nr}})}\frac{dR}{dE_{\text{nr}}} = \frac{dE_{\text{nr}}}{d(\mathcal{L}_{\text{eff}}E_{\text{nr}})}\frac{\rho_W N_T \sigma_I^{\text{as}} M_N c^2}{2M_W \mu^2}F^2(E_{\text{nr}})\int_{v_{\min}(E_{\text{nr}})}^{v_{\max}}\frac{1}{v}\frac{dn}{dv}dv, \quad (1)$$

where R is the event rate in a unit mass of the target, E_{det} is the detected energy in electron-equivalent deposited energy, E_{nr} is the nuclear recoil energy, $\mathcal{L}_{\text{eff}} = \mathcal{L}_{\text{eff}}(E_{\text{nr}})$ is a factor that converts nuclear recoil energy E_{nr} to electron-equivalent energy E_{det} relative to that of 122 keV gamma at zero electric field [20–23], ρ_W is the local mass density of dark matter (0.3 GeV/cm^3) [24], N_T is the number of target nuclei, σ_I^{as} is the asymptotic cross section for inelastic scattering at zero momentum transfer, M_N is the mass of the target nucleus, M_W is the WIMP mass, μ is the reduced mass of the WIMP mass and the target nucleus mass, $F^2(E_{\text{nr}})$ is the nuclear form factor of ^{129}Xe, $v_{\max}$ is the maximum velocity of the WIMPs in the Earth's vicinity (approximated by the local escape velocity for the galaxy, 650 km/s), $v_{\min}(E_{\text{nr}})$ is the minimum velocity the WIMP must have to be able to excite a nucleus, v is the velocity of the WIMP, and dn/dv is the velocity distribution of WIMPs. The velocity distribution, dn/dv, is assumed to be quasi-Maxwellian with the most probable thermal speed of the WIMPs being $v_0 = 220\,$km/s [26], and the average velocity of the Earth in the galactic

---

[1] This photoelectron yield is smaller than the value reported in Refs. [15,21,25], since we made a correction to the charge observed in our electronics. This correction is within the uncertainty reported earlier [15].

frame $v_e = 232$ km/s [27]. Following Refs. [12,13], the minimum velocity needed to excite ^{129}Xe is evaluated as:

$$v_{\text{min}} = v_{\text{min}}^0 + \frac{v_{\text{thr}}^2}{4v_{\text{min}}^0}, \tag{2}$$

with:

$$v_{\text{min}}^0 = \sqrt{\frac{M_N E_{\text{nr}}}{2\mu^2}} \tag{3}$$

$$E_{\text{det}} = E^* + \mathcal{L}_{\text{eff}} E_{\text{nr}} \tag{4}$$

$$v_{\text{thr}}^2 = 2\Delta E c^2/\mu, \tag{5}$$

where ΔE is the energy of the first excited state of ^{129}Xe (39.58 keV) and $E^* \sim \Delta E$ is the sum of all the energy deposited in the de-excitation process.

The total event rate in the case of a point-like target thus becomes:

$$R_{I,\text{point-like}} = \int_{v_{\text{thr}}}^{v_{\text{max}}} \frac{\rho_W v}{M_W} N_T \sigma_I(v) \frac{dn}{dv} dv = \frac{\rho_W \langle v \rangle}{M_W} f N_T \sigma_I^{\text{as}} \tag{6}$$

$$f = \frac{1}{\langle v \rangle} \int_{v_{\text{thr}}}^{v_{\text{max}}} (v^2 - v_{\text{thr}}^2)^{1/2} \frac{dn}{dv} dv, \tag{7}$$

where $\sigma_I(v)$ is the excitation cross section for a point-like target, which is expressed as the following function of the WIMP velocity v:

$$\sigma_I(v) = \frac{\mu^2}{\pi M_N} |\langle N^*|M|N \rangle|^2 \left(1 - \frac{v_{\text{thr}}^2}{v^2}\right)^{1/2} = \sigma_I^{\text{as}} \left(1 - \frac{v_{\text{thr}}^2}{v^2}\right)^{1/2}, \tag{8}$$

with $\langle N^*|M|N \rangle$ being the matrix element for inelastic scattering; details can be found in Ref. [28]. To incorporate the effects of the finite size of the ^{129}Xe nucleus, the form factor $F^2(E_{\text{nr}})$ should be taken into account. In fact, there is significant progress with regard to form factors since the DAMA results were published [29–34]. In this paper, we first choose the model of Ref. [29], which is the one used by the DAMA group [12,13], to allow for comparison with this, the only other inelastic scattering result for ^{129}Xe. Next we use the more recent calculations in Refs. [33,34] for interpreting our results in terms of a constraint on the spin-dependent WIMP–neutron cross section, which can be compared with results from elastic scattering determinations of that cross section.

The expected signals from both de-excitation and the associated nuclear recoil are simulated and then added. In the simulation, scintillation light emission due to nuclear recoil (decay constant $\tau_{\text{nr}} = 25$ ns [35]) and the subsequent γ-ray or conversion electron emission from nuclear de-excitation are simulated at their common vertex in the detector. Here we ignore the few percent difference of K shell and L shell electron ejection probability after de-excitation and gamma-ray absorption. The vertices are distributed uniformly throughout the inner detector. The half-life of the excited nuclear state can be ignored since it is much shorter ($\sim$1 ns) than the decay constant of the scintillation light. Figure 1 shows the resulting simulated energy deposits for WIMPs with various masses (a) with the form factor from Ref. [29] and (b) with the form factor from Ref. [33].

4. Data reduction and optimization

The data used for this search were taken between 24 December 2010 and 10 May 2012, and amounts to a total live time of 165.9 days. Since we took extensive calibration data and various special runs
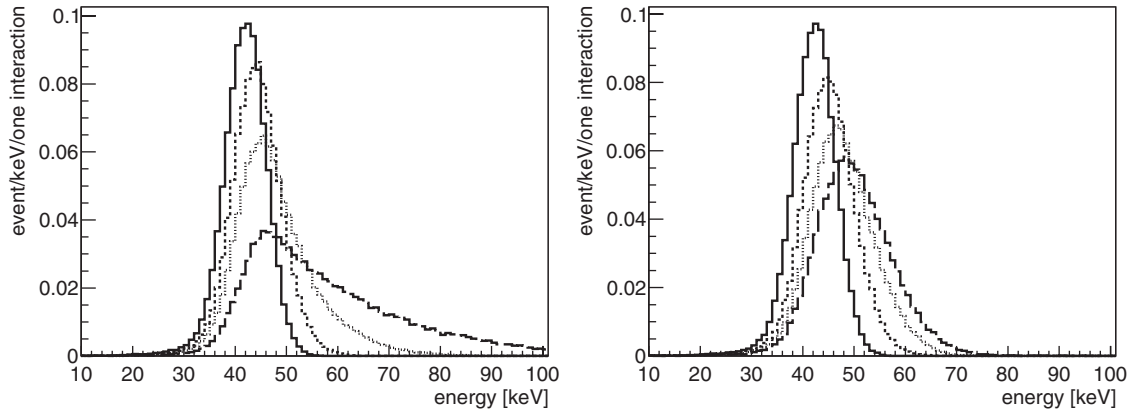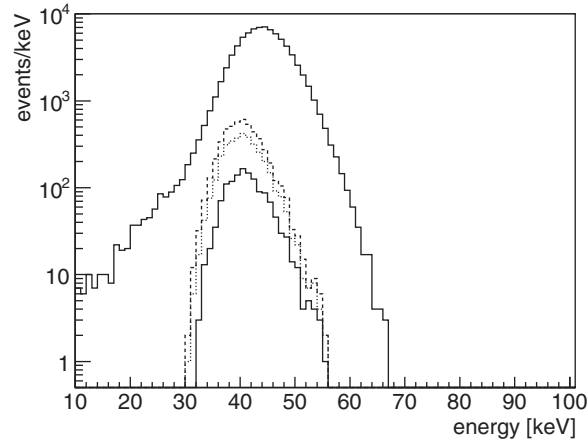
Fig. 1. Simulated energy spectra for WIMP masses of 20 (solid line), 50 (dashed line), 100 (dotted line), and 1000 GeV (long dashed line). (a) Calculated with the form factor in Ref. [29] and (b) with the form factor in Ref. [33]. In both cases it includes the energy deposited by the de-excitation gamma-ray as well as the energy deposit effected by the nuclear recoil. Our energy scale is defined by dividing the number of p.e. observed by 13.9 (p.e./keV).

to understand the background and the general detector response, we select runs taken under what we designate as "normal running conditions" with stable temperature and pressure (0.160–0.164 MPa absolute). Additional data quality checks reject runs with excessive PMT noise, unstable pedestal levels, or abnormal trigger rates.

As discussed in Refs. [21,25], most of the observed events are background events due to radioactive contamination in the aluminum seals of our PMTs and radon progeny on the inner surface of the detector. To reduce these backgrounds, a dedicated event reduction procedure was developed for this analysis. In this section we give a detailed description of this reduction procedure and our evaluation of its acceptance.

This dedicated data reduction proceeds in four steps: (1) Pre-selection. This is similar to Ref. [21]. The difference is that events occurring less than 10 ms prior to the one under consideration are also rejected since events caused by ^{214}Bi decay, a daughter of ^{222}Rn, must be removed. (2) Fiducial volume (radius) cut. As is described in Ref. [15], the observed pattern of p.e. is used to reconstruct an event vertex. The radial position R of an event is obtained from this reconstruction. (3) Timing cut. Even after the radius cut, some surface events remain in the sample. Timing information is used to further reduce these remaining surface background events. Here we use the timing difference δT_m between the first hit and an average of hit timings of first 50% of an event's remaining hits—after discarding the next ten following that first one. A larger timing difference is indicative of a surface event that was mistaken for a fiducial volume event. (4) Band cut. Grooves and gaps exist between PMTs. Scintillation light caused by events inside these grooves projects onto the inner surface of the XMASS detector in a characteristic band pattern. This pattern emerges because the propagation of scintillation light from within a straight groove is constrained by the rims of that groove acting as a slit projecting a characteristic band shape that is recognized by our software. Events with such a pattern are eliminated by this cut. Using the band identified by our software, we cut on the ratio of charges contained in that band to the total charge in the event:

$$\text{Band cut parameter } F_B = \frac{\text{p.e. in the band of width 15 cm}}{\text{Total p.e. in the event}}. \tag{9}$$

Fig. 2. Energy spectra of the simulated events after each reduction step. As an example we chose a WIMP mass of 50 GeV and the form factor in Ref. [29]. From top to bottom, simulated energy spectrum after pre-selection (solid line), cut (2) (dashed line), cut (3) (dotted line), and cut (4) (solid line). As we do not apply the proper radial correction for energy, a shift in our energy scale seems to occur after our fiducial volume cut (2). As we are only using events in a very limited fiducial volume and our energy scale is based on calibration at the center of the detector, the energy scale of the surviving events is correct within 4%.
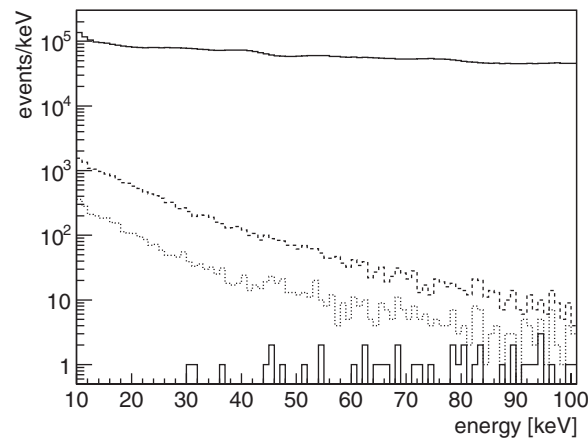
Fig. 3. Energy spectra of the observed events after each reduction step for our 165.9 live days of data. From top to bottom, the observed energy spectrum after pre-selection (solid line), cut (2) (dashed line), cut (3) (dotted line), and cut (4) (solid line). The fiducial volume contains 41 kg of LXe.

The cut values for the three cuts that are applied after our almost standard pre-selection were optimized for a WIMP mass of 50 GeV. Except for the radius cut, our cut values were determined by optimizing the ratio of simulated signal events surviving the cuts in a tentative signal range from 30 to 80 keV over the sum of background events found in the data in two side bands ranging from 10 to 30 and from 80 to 100 keV. For the radius cut, this procedure results in an extremely low fiducial volume, leading us to halt this optimization at 15 cm. For the remaining cuts, the values resulting from our optimization were 12.91 ns for the timing cut and a ratio of 0.248 for the band cut. Events with parameter values smaller than these cut values enter into the final sample.

Figures 2 and 3 show the impact of our cuts on the expected signal from our 50 GeV WIMP simulation and the observed data spectrum, respectively. The signal window is defined so that it contains 90% of the simulated 50 GeV WIMP signal with equal 5% tails to either side, which results in a 36–48 keV window. While the underlying simulation shown in Fig. 2 is based on the form factors

Table 1. Signal efficiencies with their systematic errors for deriving the limit shown in Figs. 4 and 7. The row starting from (a) is based on Ref. [29], and the one starting from (b) on Ref. [33].

| WIMP mass (GeV)	20	50	100	300	1000	3000	5000
(a) signal efficiency (%)	$23 \pm^7_6$	$29 \pm^4_5$	$26 \pm^2_4$	$19 \pm^1_3$	$16 \pm^1_3$	$15 \pm^1_3$	$15 \pm^1_3$
(b) signal efficiency (%)	$24 \pm^7_6$	$30 \pm^2_5$	$29 \pm^2_4$	$26 \pm^2_5$	$25 \pm^2_5$	$25 \pm^2_5$	$25 \pm^2_5$

used in Ref. [29], it can be seen in Fig. 1 that the shape of this distribution for a 50 GeV WIMP does not change much with the use of the more modern form factors. These cut values and the signal window optimized for the 50 GeV WIMPs were also used to obtain the limits for the other WIMP masses. Our signal efficiency is defined as the ratio between the number of simulated events remaining after all cuts in the 36–48 keV signal region and the number of simulated events generated within the fiducial volume (radius less than 15 cm, containing 41 kg of LXe). As shown in Table 1, signal efficiency ranges from 29% for 50 GeV WIMPs to 15% for 5 TeV WIMPs for the nuclear form factors given in Ref. [29].

5. Results and discussion

As clearly visible in Fig. 3, the cuts discussed in the previous section almost eliminate all background in and around the signal window. After all cuts, 5 events remain in our 36–48 keV signal region. The main contribution to the remaining background in this energy region stems from the ^{222}Rn daughter ^{214}Pb. From our simulation we estimate this background alone to contribute 2.0 ± 0.6 events. As other background contributions are smaller but less certain, we do not subtract background when calculating our limits. Our detector's low background allows us to directly use the event count in the signal region to extract our limit on the inelastic scattering cross section of WIMPs on ^{129}Xe nuclei. Using Eq. 6 and taking into account the nuclear form factor and our signal efficiency we derive a 90% C.L. upper limit for this cross section, which in Fig. 4 is compared to the result from Refs. [12,13]. The gray band reflects our systematic uncertainties. The systematic uncertainty on
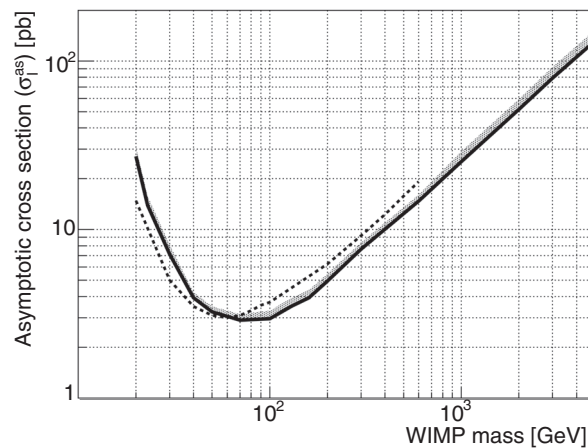
Fig. 4. The black solid line is our 90% C.L. upper limit on the asymptotic cross section σ_i^{as} for inelastic scattering on ^{129}Xe using the same form factors as DAMA. The gray band covers its variation with our systematic uncertainty. The dotted line is the limit obtained by the DAMA group [12,13]. It was derived after statistically subtracting background. Our low background allows us to derive this limit without such background subtraction.
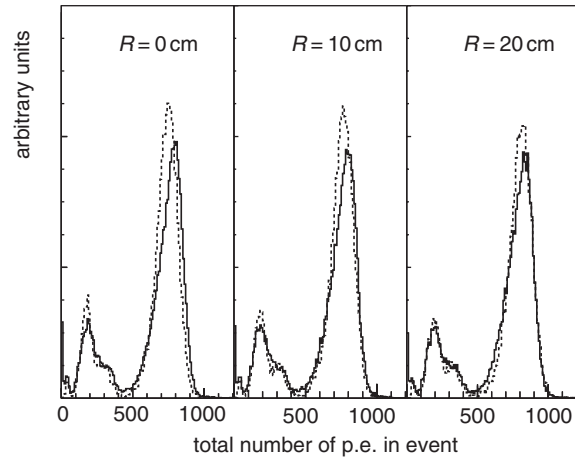
Fig. 5. Comparison between data (solid histograms) and simulation (dashed histograms) of the energy distribution of ^{241}Am at three radial positions R.
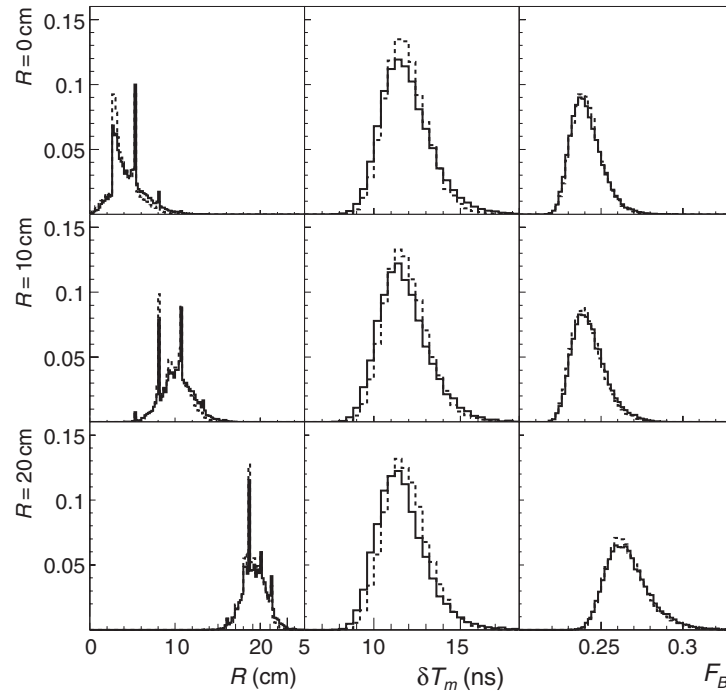
Fig. 6. Comparison between ^{241}Am data (solid histograms) and simulation (dashed histograms) for the three cut parameters at three radial positions in the detector, $R = 0$ cm, 10 cm, and 20 cm, from top to bottom, respectively. From left to right the distributions for all three parameters, the reconstructed radius, the timing difference, and the band cut parameter, are shown for each of the source positions.

our signal efficiency is estimated from data–MC comparisons for ^{241}Am calibration data (60 keV) at various positions within the fiducial volume. The relevant comparisons are shown in Figs. 5 and 6. From these comparisons we derive the systematic uncertainties in energy scale, energy resolution, radius reconstruction, timing cut, and band cut parameter. There is also uncertainty in the effective light yield $\mathcal{L}_{\text{eff}}$ and the decay constants of nuclear recoils. The cumulative effect of these individual contributions is obtained by summation in quadrature.

Table 2. Systematic error of the signal efficiency for different WIMP masses. As in the previous table, (a) is for the signal calculation based on Ref. [29] and (b) on Ref. [33]. All the entries are in % of the nominal efficiencies. See text for details. ^{241}Am data and simulated events (see text).

(a) WIMP mass (GeV)	20	50	100	300	1000	3000	5000
Energy scale	$\pm^{30}_{22}$	$\pm^{11}_{13}$	$\pm^{0}_{5.1}$	$\pm^{0.4}_{7.1}$	$\pm^{1.1}_{9.5}$	$\pm^{2.2}_{11}$	$\pm^{2.7}_{11}$
Energy resolution	$\pm^{0}_{8.2}$	$\pm^{0}_{5.6}$	$\pm^{0}_{6.8}$	$\pm^{0}_{8.1}$	$\pm^{0}_{9.7}$	$\pm^{0}_{8.8}$	$\pm^{0}_{9.0}$
Radius cut	$\pm^{0}_{3.3}$	$\pm^{0}_{3.2}$	$\pm^{0}_{4.0}$	$\pm^{0}_{5.2}$	$\pm^{0}_{6.8}$	$\pm^{0}_{6.3}$	$\pm^{0}_{6.4}$
Timing cut	$\pm^{4.2}_{5.1}$	$\pm^{4.2}_{5.1}$	$\pm^{4.2}_{5.1}$	$\pm^{4.2}_{5.1}$	$\pm^{4.2}_{5.1}$	$\pm^{4.2}_{5.1}$	$\pm^{4.2}_{5.1}$
Band cut	± 4.2	± 4.2	± 4.2	± 4.2	± 4.2	± 4.2	± 4.2
$\mathcal{L}_{\text{eff}}$	$\pm^{6.4}_{0}$	$\pm^{1.4}_{0.2}$	$\pm^{0}_{1.4}$	$\pm^{3.9}_{0}$	$\pm^{1.0}_{1.3}$	$\pm^{0}_{1.7}$	$\pm^{0}_{4.0}$
τ_{nr}	$\pm^{0}_{0.8}$	$\pm^{1.3}_{2.2}$	$\pm^{0}_{8.8}$	$\pm^{0}_{4.6}$	$\pm^{0}_{4.7}$	$\pm^{0}_{5.7}$	$\pm^{0}_{5.7}$
Total systematic error	$\pm^{31}_{25}$	$\pm^{13}_{16}$	$\pm^{5.9}_{15}$	$\pm^{7.1}_{14}$	$\pm^{6.0}_{17}$	$\pm^{6.3}_{18}$	$\pm^{6.5}_{18}$
(b) WIMP mass (GeV)	20	50	100	300	1000	3000	5000
Energy scale	$\pm^{27}_{21}$	$\pm^{5.6}_{9.9}$	$\pm^{0}_{7.8}$	$\pm^{4.8}_{13}$	$\pm^{5.5}_{14}$	$\pm^{5.9}_{14}$	$\pm^{6.1}_{17}$
Energy resolution	$\pm^{0}_{7.1}$	$\pm^{0}_{5.7}$	$\pm^{0}_{7.9}$	$\pm^{0}_{8.9}$	$\pm^{0}_{9.7}$	$\pm^{0}_{9.5}$	$\pm^{0}_{9.5}$
Radius cut	$\pm^{0}_{3.7}$	$\pm^{0}_{4.1}$	$\pm^{0}_{4.4}$	$\pm^{0}_{4.3}$	$\pm^{0}_{5.3}$	$\pm^{0}_{4.5}$	$\pm^{0}_{3.9}$
Timing cut	$\pm^{4.2}_{5.1}$	$\pm^{4.2}_{5.1}$	$\pm^{4.2}_{5.1}$	$\pm^{4.2}_{5.1}$	$\pm^{4.2}_{5.1}$	$\pm^{4.2}_{5.1}$	$\pm^{4.2}_{5.1}$
Band cut	± 4.2	± 4.2	± 4.2	± 4.2	± 4.2	± 4.2	± 4.2
$\mathcal{L}_{\text{eff}}$	$\pm^{0}_{2.0}$	$\pm^{0}_{1.5}$	$\pm^{1.8}_{0}$	$\pm^{5.7}_{0}$	$\pm^{1.0}_{0}$	$\pm^{2.2}_{2.9}$	$\pm^{5.1}_{0}$
τ_{nr}	$\pm^{0}_{0.8}$	$\pm^{0}_{4.7}$	$\pm^{0}_{5.4}$	$\pm^{0}_{4.7}$	$\pm^{0.2}_{4.1}$	$\pm^{0}_{7.1}$	$\pm^{0}_{4.9}$
Total systematic error	$\pm^{28}_{24}$	$\pm^{8.2}_{15}$	$\pm^{6.2}_{15}$	$\pm^{9.5}_{18}$	$\pm^{8.2}_{19}$	$\pm^{8.7}_{20}$	$\pm^{9.9}_{21}$

As an example of our systematic error evaluation, we explain it here for the signal efficiency for 50 GeV WIMPs; see Table 2 for other masses. The uncertainty in our energy scale evaluates to $\pm^{4.6}_{3.1}$% by comparing more than 10 sets of calibration data (^{57}Co), taken at different times throughout the data-taking period, with our simulation. Changing the number of photons generated per unit energy deposited in the simulation by this amount, the signal efficiency changes by $\pm^{11}_{13}$%. The uncertainty in the energy resolution, 12%, is evaluated by comparing the resolution of the 60 keV peak in the calibration data and simulated events. This leads to a 5.6% reduction in the signal efficiency. The radial position of the reconstructed vertex for the calibration data differs by 5 mm from the true source position, which causes a 3.2% reduction in efficiency. The band cut and the timing cut each have a slightly different impact on calibration data and simulated events. By taking the difference of their acceptance, we evaluated their systematic impact on the signal efficiency to ± 4.2% for the band cut and $\pm^{4.2}_{5.1}$% for the timing cut. The 1 σ uncertainty in the effective light yield $\mathcal{L}_{\text{eff}}$ as evaluated in Ref. [20] changes the signal efficiency in a range from +1.4% to −0.2%. For the decay constants of scintillation light caused by nuclear recoils we took the uncertainty in the determination of the constants and the difference between our values and the NEST model [36,37], ± 1 ns, as our systematic uncertainty. The total systematic error on the signal efficiency for a 50 GeV WIMP is evaluated to $\pm^{13}_{16}$%, summing up in quadrature the systematic errors as detailed above. This evaluation was repeated for WIMP masses of 20, 100, and 300 GeV and 1, 3, and 5 TeV, and is assumed to be applicable for masses close to the ones evaluated.

Finally, we evaluate the impact of our systematic uncertainty on the limit we obtain. Assuming a true number of events μ in the energy window before the event reduction, we can calculate the expected number of observed events by multiplying with the signal efficiency tabulated in Table 1. Based on the expected number of observed events, we can generate the number of observed events
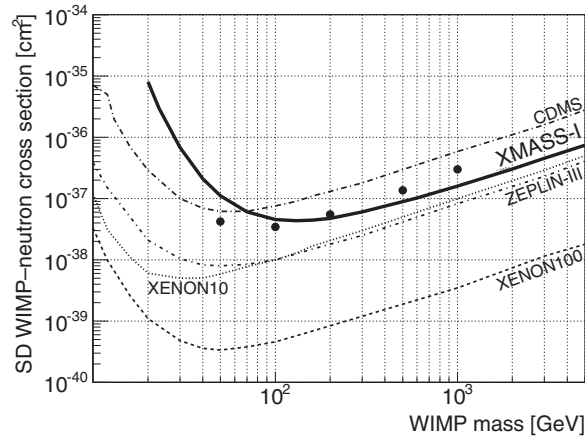
Fig. 7. The thick line with its gray shaded systematic uncertainty band represents our limit using the form factors of Ref. [33], and the dots represent our limits following Ref. [34] for that paper's choice of WIMP masses. The dashed, dotted, dash-dotted, and long dash-dotted lines represent experimental constraints on spin-dependent WIMP nucleon cross sections extracted from elastic scattering data as published in Refs. [38–41], respectively. Our own limit is the first derived exclusively from data on inelastic scattering.

following Poisson statistics. This procedure was repeated to accumulate a histogram of the observed number of events for a fixed μ by sampling the signal efficiency within its systematic error. The 90% C.L. upper limit for μ is the one that results in a 10% probability of having five events or fewer. Using Eq. 6, this is then translated to an inelastic WIMP nucleus cross section, and the variation of our limit within our systematic uncertainties. Both are shown by the black line and gray band in Fig. 4, respectively.

It should be noted that the constraint obtained by the DAMA group [12,13] was derived from a statistical evaluation of an excess above a large background of $2 \times 10^{-2}\,\mathrm{keV}^{-1}\,\mathrm{d}^{-1}\,\mathrm{kg}^{-1}$. We achieved a lower background $\sim 3 \times 10^{-4}\,\mathrm{keV}^{-1}\,\mathrm{d}^{-1}\,\mathrm{kg}^{-1}$ using the cut discussed above. This low background allowed us to avoid having to subtract background to obtain a competitive limit.

Our limits that are based on the updated nuclear form factors given in Refs. [33,34] are also using the same data reduction and therewith event sample as those for the older form factors. The results shown in Fig. 7 are based on the inelastic structure factors for $S_n(u)$ 1b+2b currents as shown in Fig. 1 of Ref. [33], and on the time-averaged differential scattering rate for inelastic scattering as shown in Fig. 4 of Ref. [34], the latter taken with a normalization of 17 fb[2] for the total WIMP–nucleon cross section. Figure 7 also shows previous experimental limits for the spin-dependent WIMP–neutron cross section that were previously obtained by XENON10, CDMS, ZEPLIN-III, and XENON100 [38–41]. All of these existing limits are based on spin-dependent elastic scattering, while our analysis explicitly restricts itself to inelastic scattering on a nucleus.

6. Conclusion

A search for inelastic scattering of WIMPs on ^{129}Xe was performed using data from our single-phase liquid-xenon detector XMASS. Events reconstructed in a spherical fiducial volume of 15 cm radius at the center of the detector containing 41 kg of LXe were used in this analysis. We observed no significant excess in 165.9 live days' data and derived for e.g. a 50 GeV WIMP an upper limit of 3.2 pb at the 90% confidence level for its inelastic cross section on ^{129}Xe nuclei using the form

---

[2] This value was taken from Ref. [34]'s Ref. [46] and confirmed with one of the authors of Ref. [34].

factors of Ref. [29] and an upper limit for the spin-dependent WIMP–neutron cross section of 110 fb or 42 fb, respectively, using the updated form factors from Refs. [33] or [34].

References

[1] R. Bernabei et al., Eur. Phys. J. C **56**, 333 (2008).
[2] R. Bernabei et al., Eur. Phys. J. C **67**, 39 (2010).
[3] C. E. Aalseth et al., Phys. Rev. Lett. **106**, 131301 (2011).
[4] G. Angloher et al., Eur. Phys. J. C **72**, 1971 (2012).
[5] E. Aprile et al., Phys. Rev. Lett. **109**, 181301 (2012).
[6] J. Angle et al., Phys. Rev. Lett. **107**, 051301 (2011).
[7] Z. Ahmed et al., Science **327**, 1619 (2010).
[8] Z. Ahmed et al., Phys. Rev. Lett. **106**, 131302 (2011).
[9] E. Armengaud et al., Phys. Rev. D **86**, 051701(R) (2012).
[10] H. Ejiri, K. Fushimi, and H. Ohsumi, Phys. Lett. B **317**, 14 (1993).
[11] K. Fushimi et al., Nucl. Phys. B Proc. Suppl. **35**, 400 (1994).
[12] P. Belli et al., Phys. Lett. B **387**, 222 (1996).
[13] R. Bernabei et al., New J. Phys. **2**, 15 (2000).
[14] Y. Suzuki, arXiv:0008296 [hep-ph].
[15] K. Abe et al. (XMASS Collaboration), Nucl. Instrum. Meth. A **716**, 78 (2013).
[16] S. Fukuda et al. (Super-Kamiokande Collaboration), Nucl. Instrum. Meth. A **501**, 418 (2003).
[17] S. Agostinelli et al., Nucl. Instrum. Meth. A **506**, 250 (2003).
[18] K. Amako et al., IEEE Trans. Nucl. Sci. **53**, 270 (2006).
[19] D. Akimov et al., Phys. Lett. B **524**, 245 (2002).
[20] E. Aprile et al., Phys. Rev. Lett. **107**, 131302 (2011).
[21] K. Abe et al. (XMASS Collaboration), Phys. Lett. B **719**, 78 (2013).
[22] A. Manzur et al., Phys. Rev. C **81**, 025808 (2010).
[23] E. Aprile et al., Phys. Rev. D **88**, 012006 (2013).
[24] J. Beringer et al. (Particle Data Group), Phys. Rev. D **86**, 010001 (2012).
[25] K. Abe et al. (XMASS Collaboration), Phys. Lett. B **724**, 46 (2013).
[26] G. Jungman et al., Phys. Rep. **267**, 195 (1996).
[27] K. Freese et al., Phys. Rev. D **37**, 3388 (1988).
[28] J. Ellis et al., Phys. Lett. B **212**, 375 (1988).
[29] J. Engel, Phys. Lett. B **264**, 114 (1991).
[30] P. Toivanen et al., Phys. Lett. B **666**, 1 (2008).
[31] P. Toivanen et al., Phys. Rev. C **79**, 044302 (2009).
[32] P. Klos et al., Phys. Rev. D **88**, 083516 (2013).
[33] L. Baudis et al., Phys. Rev. D **88**, 115014 (2013).
[34] J. D. Vergados, H. Ejiri, and K. G. Savvidy, Nucl. Phys. B **877**, 36 (2013).
[35] K. Ueshima, Study of pulse shape discrimination and low background techniques for liquid xenon dark matter detectors, *Ph.D. Thesis*, University of Tokyo (2010).
[36] M. Szydagis et al., J. Instrum. **6**, P10002 (2011).
[37] NEST (Noble Element Simulation Technique). (Available at: http://nest.physics.ucdavis.edu/site/, date last accessed May 10, 2014).
[38] E. Aprile et al., Phys. Rev. Lett. **111**, 021301 (2013).
[39] J. Angle et al., Phys. Rev. Lett. **101**, 091301 (2008).
[40] Z. Ahmed et al., Phys. Rev. Lett. **102**, 011301 (2009).
[41] D. Akimov et al., Phys. Lett. B. **709**, 14 (2012).